

Sheets, filaments and clumps - high resolution simulations of how the thermal instability can form molecular clouds

C. J. Wareing^{1*}, S. A. E. G. Falle² and J. M. Pittard¹

¹*School of Physics and Astronomy, University of Leeds, Leeds, LS2 9JT, U.K.*

²*School of Mathematics, University of Leeds, Leeds, LS2 9JT, U.K.*

Accepted 2019 March 6. Received 2019 February 19; in original form 2018 December 21

ABSTRACT

This paper describes 3D simulations of the formation of collapsing cold clumps via thermal instability inside a larger cloud complex. The initial condition was a diffuse atomic, stationary, thermally unstable, 200 pc diameter spherical cloud in pressure equilibrium with low density surroundings. This was seeded with 10% density perturbations at the finest initial grid level (0.29 pc) around $n_{\text{H}}=1.1 \text{ cm}^{-3}$ and evolved with self-gravity included. No magnetic field was imposed. Resimulations at a higher resolution of a region extracted from this simulation (down to 0.039 pc), show that the thermal instability forms sheets, then filaments and finally clumps. The width of the filaments increases over time, in one particular case from 0.26 to 0.56 pc. Thereafter clumps with sizes of around 5 pc grow at the intersections of filaments. 21 distinct clumps, with properties similar to those observed in molecular clouds, are found by using the FellWalker algorithm to find minima in the gravitational potential. Not all of these are gravitationally bound, but the convergent nature of the flow and increasing central density suggest they are likely to form stars. Further simulation of the most massive clump shows the gravitational collapse to a density $> 10^6 \text{ cm}^{-3}$. These results provide realistic initial conditions that can be used to study feedback in individual clumps, interacting clumps and the entire molecular cloud complex.

Key words: instabilities – ISM: structure – ISM: clouds – ISM: molecules – stars: formation – methods: numerical

1 INTRODUCTION

Extensive studies of the nearest star-forming clouds, most recently with the *Herschel* Space Observatory have revealed that every interstellar cloud contains an intricate network of interconnecting filamentary structures (see, for example, Section 2 of the review of André et al. 2014, and references therein). The data, from *Herschel* and near-IR studies for example, suggest a scenario in which these ubiquitous filaments represent a key step in the star formation process: large-scale flows compress the diffuse ISM and form molecular clouds; an interconnecting filamentary structure forms within these clouds; magnetic fields affect the flow of material and hence overall structure, although do not appear to set the central densities in the filaments; gravity plays an increasingly important role, fragmenting the filaments once they are cold and dense into prestellar cores and finally protostars, commonly occurring at the intersections or hubs of the intricate structure.

Observational results now connect well with numeri-

cal simulations, as highlighted in Section 5 of André et al. (2014) and references therein. Early numerical simulations showed that gas is rapidly compressed into a hierarchy of sheets and filaments, without the aid of gravity (Bastien 1983; Porter, Pouquet & Woodward 1994; Vázquez-Semadini 1994; Padoan et al. 2001). Turbulent box simulations and colliding flows produce filaments (e.g. Mac Low & Klessen 2004; Hennebelle et al. 2008; Federrath et al. 2010; Gómez & Vázquez-Semadini 2014; Moeckel & Burkert 2015; Smith, Glover & Klessen 2014; Kirk et al. 2015). Hennebelle & André (2013) demonstrated the formation of filaments through the velocity shear that is common in magnetised turbulent media. Other authors have explained filaments as the stagnation regions in turbulent media (Padoan et al. 2001). The formation of filaments preferentially perpendicular to the magnetic field lines is possible in strongly magnetised clouds (Li et al. 2010; Wareing et al. 2016). André et al. (2014) note that the same 0.1 pc filament width is measured for low-density, subcritical filaments suggesting that this characteristic scale is set by the physical processes producing the filamentary structure. Furthermore, they note that at least in the case of diffuse gravitationally unbound clouds

* E-mail: C.J.Wareing@leeds.ac.uk

(e.g. Polaris), gravity is unlikely to be involved. Large-scale compression flows, turbulent or otherwise, provide a potential mechanism, but it is not clear why any of these would produce filaments with a constant radius.

Smith, Glover & Klessen (2014) examined the influence of different types of turbulence, keeping the initial mean density constant in simulations without magnetic fields. They found that when fitted with a Plummer-like profile, the simulated filaments are in excellent agreement with observations, with shallow power-law profile indexes of $p \approx 2.2$, without the need for magnetic support. They found an average FWHM of ≈ 0.3 pc, when considering regions up to 1 pc from the filament centre, in agreement with predictions for accreting filaments. Constructing the fit using only the inner regions, as in *Herschel* observations, they found a resulting FWHM of ≈ 0.2 pc.

Kirk et al. (2015) used the FLASH hydrodynamics code to perform numerical simulations of turbulent cluster-forming regions, varying density and magnetic field. They used HD and MHD simulations, initialised with a supersonic ($M \approx 6$) and super-Alfvénic ($M_A \approx 2$) turbulent velocity field, chosen to match observations, and identified filaments in the resulting column density maps. They found magnetic fields have a strong influence on the filamentary structure, tending to produce wider, less centrally peaked and more slowly evolving filaments than in the hydrodynamic case. They also found the magnetic field is able to suppress the fragmentation of cores, perhaps somewhat surprisingly with super-Alfvénic motion involved in the initial condition. Overall, they noted the filaments formed in their simulations have properties consistent with the observations they set out to reproduce, in terms of radial column density profile, central density and inner flat radius.

Numerical simulations now include the thermodynamic behaviour of the cloud material, magnetic fields, gravity and feedback from massive stars, both radiative and dynamic (Beuther, Linz & Henning 2008; Harper-Clark & Murray 2009; Krumholz & Matzner 2009; Gray & Scannapieco 2011; Koenig et al. 2012; Rogers & Pittard 2013, 2014; Gatto et al. 2015; Offner & Arce 2015; Walch & Naab 2015; Walch et al. 2015; Girichidis et al. 2015; Körtgen et al. 2016). Supersonic, trans-Alfvénic turbulence has emerged as an ingredient which can, when injected at the right scale, result in the formation of filaments which possess properties remarkably similar to those derived from observational results whilst also reproducing the observed relatively smooth nature of the magnetic field. The interested reader is referred to lengthy introductions and reviews in the first sections of previous works by the same authors (Wareing et al. 2016, 2017a,b, 2018).

The work presented here continues the exploration of the formation of clumps connected by filamentary structures through the use of hydrodynamic simulations of the thermal instability (Parker 1953; Field 1965). A number of authors have investigated analytically the effects of different mechanisms on the thermal instability (Birk 2000; Nejad-Asghar & Ghanbari 2003; Stiele, Lesch & Heitsch 2006; Fukue & Kamaya 2007; Shadmehri 2009). Other groups have numerically investigated flow-driven molecular cloud formation including the effects of the thermal instability (e.g. Lim, Falle & Hartquist 2005; Vázquez-Semadini et al. 2007; Hennebelle et al. 2008; Heitsch, Stone & Hartmann 2009; Ostriker, Mc-

Kee & Leroy 2010; Van Loo, Falle & Hartquist 2010; Inoue & Inutsuka 2012). Hennebelle & Audit (2007) and Hennebelle et al. (2007) showed that HI clouds formed by thermal instability can explain a variety of observational characteristics. Inoue & Inutsuka (2012) used 3D MHD simulations, including radiative cooling and heating, to investigate the formation of molecular clouds. They consider the scenario of accretion of HI clouds and the piling up of the initial HI medium behind shock waves induced by accretion flows in order to form a molecular cloud. They find the resulting timescale of molecular cloud formation of ~ 10 Myr is consistent with the evolutionary timescale of the molecular clouds in the LMC (Kawamura et al. 2009). This numerical work has included magnetic fields, self-gravity and the thermal instability and has identified the thermal and dynamical instabilities that are responsible for the rapid fragmentation of the nascent cloud, largely through flow-driven scenarios.

Here we concentrate on the thermal instability itself without any initial flow in a low-density cloud of quiescent diffuse medium initially in the unstable phase. The cloud is in pressure equilibrium with its lower-density (thus temperature above equilibrium) surroundings and we include accurate thermodynamics and self-gravity. In particular, the aim is to discern whether thermal instability alone can create high enough density structure that gravity can then dominate and drive the eventual collapse of the clump to form clusters of stars, regardless of the apparent status of the energy budget. This has not been observed in our previous works. Subsequent aims are to confirm whether such clumps display realistic properties when compared to observationally-derived properties, and whether mergers and collisions of clumps reproduce observations. The simulations presented herein are also intended as a means to define realistic initial conditions for cluster feedback simulations.

In the next section the initial condition for this high resolution study is described. In Section 3, the numerical method and model are discussed. Results are discussed in the following sections. Specifically, the evolution of the whole cloud is discussed in Section 4. The state of the cloud complex and the clumps identified within are discussed in Section 5. Density and velocity power spectra of the cloud at this time and an individual clump are presented in Section 6 and the final gravitational collapse of the most massive clump is discussed in Section 7. The work is summarised and concluded in Section 8, which also sets out how details of the simulations may be used in future works.

2 INITIAL CONDITIONS

Our recent work (Wareing et al. 2016, 2017a,b, 2018) has highlighted the way that the thermal instability (Field 1965), under the influence of gravity and realistic magnetic fields (magnetic pressure) in the ideal magnetohydrodynamic (MHD) limit, can drive the evolution of diffuse thermally unstable warm clouds from a pressure-supported quiescent low-density state to form high-density, cold (≤ 100 K) clumps and, in the presence of magnetic field, sheet-like structures that are filamentary in appearance, perpendicular to the applied field (Wareing et al. 2016, hereafter Paper I).

In our most recent work (Wareing et al. 2018, hereafter

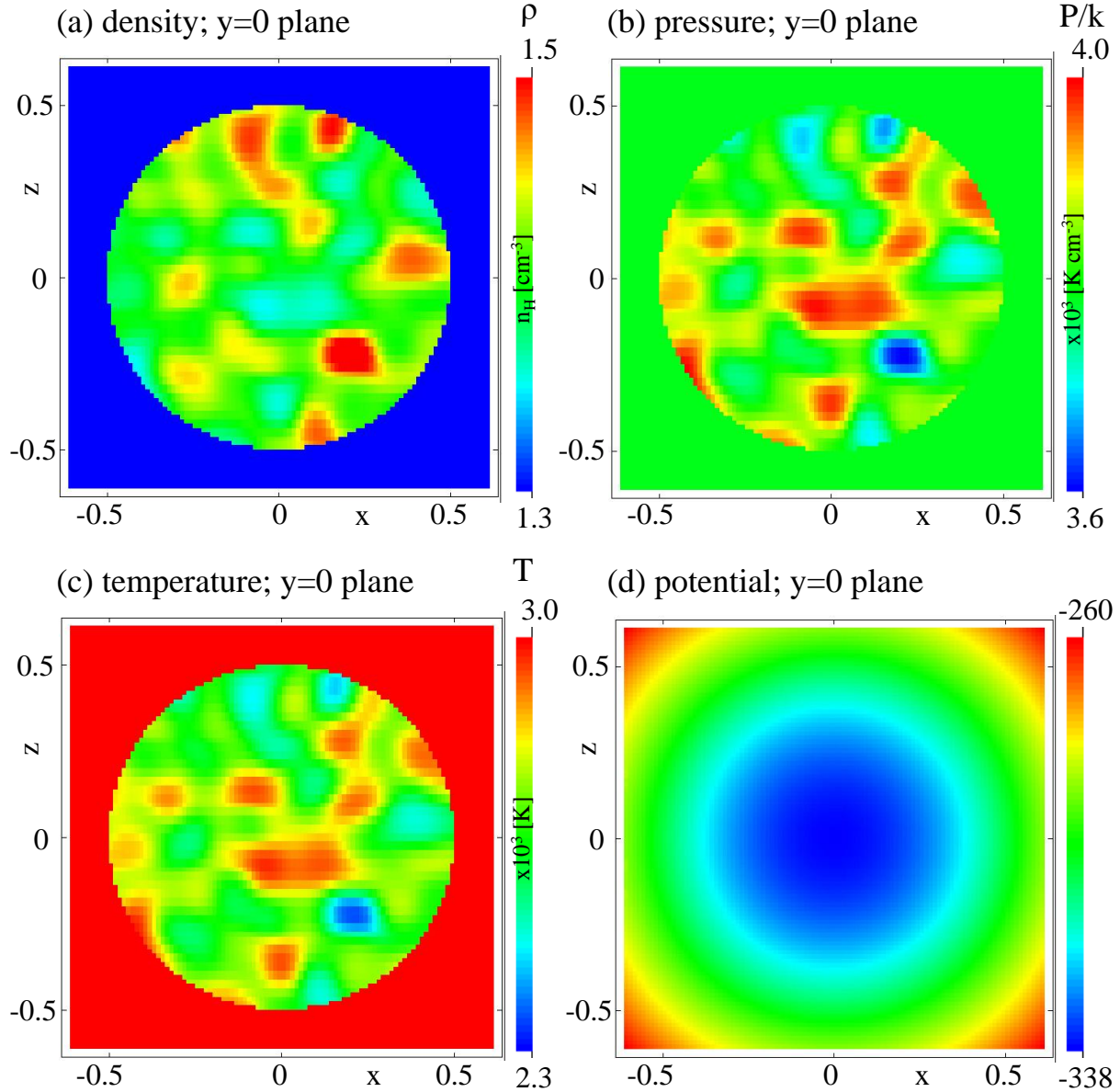


Figure 1. Initial conditions in the Model 1 simulation. The appearance of the extracted region of the Paper IV HD simulation on the $y = 0$ plane, surrounded by the ambient pressure-matched stable conditions, imposed in the Model 1 simulation. The region was extracted at $t=16.2$ Myrs of the Paper IV HD simulation. The unit of distance is 50 pc. Raw data is available from <https://doi.org/10.5518/483>.

Paper IV), the model of stellar wind feedback in a sheet-like structure first considered in Wareing et al. (2017a, hereafter Paper II) was applied to the Rosette Nebula, solving outstanding issues around the age and size of the nebula (Bruhweiler et al. 2010). The calculations in Paper IV explored both hydrodynamic (HD) and MHD initial conditions. The computational domain extended from -150 pc to +150 pc in all three Cartesian xyz directions. A diffuse cloud with an average number density of atomic hydrogen of $n_H = 1.1$ cm $^{-3}$ and radius $r=100$ pc was placed at the centre of the domain (0,0,0). The cloud was seeded with random density variations of 10% about its average density. The cloud mass was 135,000 M_\odot . Initial pressure was set according to the (unstable) equilibrium of heating and cooling at $P_{eq}/k = 4700 \pm 300$ K cm $^{-3}$, resulting in an initial cloud tempera-

ture $T_{eq} = 4300 \pm 700$ K. External to the cloud the density was reduced by a factor of 10 to $n_H = 0.1$ cm $^{-3}$, but the external pressure matched the cloud ($P_{eq}/k = 4700$ K cm $^{-3}$). The external medium was prevented from cooling or heating, keeping this pressure throughout the simulation. No magnetic field or velocity structure was introduced in the HD case. When the simulation was evolved, condensations due to the thermal instability began to grow in the cloud and after 16 Myrs their densities were ~ 40 per cent greater than the initial average density of the cloud.

In the present work, the central region of Paper IV Simulation 1, the HD simulation, has been extracted at a simulation time of 16 Myrs, placed in ambient pressure-matched surroundings and then evolved at higher resolution in order to study the cloud complex formed and to determine the na-

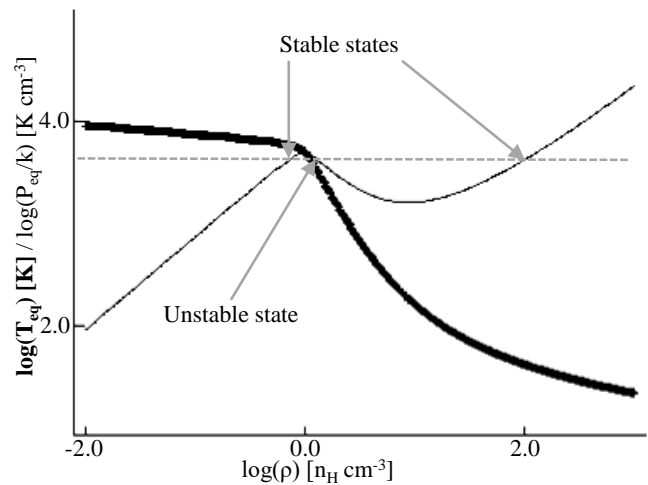
Table 1. Suite of 3D Cartesian hydrodynamic simulations with self-gravity performed in this work. Details of the HD Simulation in Paper IV, from which the central region is extracted for resimulation in this work, are provided for reference.

Name	Domain pc on a side	G0 # of cells	Levels of AMR	t_{start} [Myr]	Resolution [pc]	HD /MHD?	Cooling?	Heating?	Gravity?
Paper IV HD (Wareing et al. 2018)	300	$8 \times 8 \times 8$	8	0.0	0.29	HD	Y	Y	Y
Model 1	100	$10 \times 10 \times 10$	6	16.2	0.3125	HD	Y	Y	Y
Model 2	100	$10 \times 10 \times 10$	7	21.7	0.156	HD	Y	Y	Y
Model 3	100	$10 \times 10 \times 10$	8	21.7	0.078	HD	Y	Y	Y
Model 4	100	$10 \times 10 \times 10$	9	22.8	0.039	HD	Y	Y	Y
Clump	10	$10 \times 10 \times 10$	7	44	0.0156	HD	Y	Y	Y

ture of the clumps therein. The aim is to explore how gravity takes over from the effect of thermal instability, without the extra complexity of magnetic field at this stage. If thermal instability, subsequently dominated by gravity is able to create truly star-forming collapsing clumps with realistic properties, then a particularly simple scenario for the formation of stars is presented. Simulations in a future work will examine the role of magnetic field in the formation of cloud complexes and collapsing molecular substructure. The average pressure across the cloud in the Paper IV HD simulation had decreased from the initial pressure to levels around $P/k = 3800 \pm 200 \text{ K cm}^{-3}$. In the Paper IV HD simulation, this decrease in cloud pressure compared to the over-pressured surroundings resulted in a compression of the cloud by the surrounding medium. Isolating the study of the thermal instability from this effect is the secondary reason, after allowing for higher resolution, for extracting the 25 pc-radius sphere centred on (0,0,0) in this new simulation.

A slice through the centre of the new domain, containing the extracted section within $r \leq 0.5$ (25 pc) is shown in Fig 1. The new domain extends to -1 and +1 (-50 pc to +50 pc) in all three Cartesian directions. The pressure and hence density outside the extracted region is defined by matching the average pressure across the central region to the equivalent stable equilibrium state density of $n_H = 0.643 \text{ cm}^{-3}$ with the same pressure. The pressure-equivalent stable and unstable states are explicitly indicated in Fig 2. The surrounding medium is uniform and stationary. The total mass in the entire domain is approximately $20,000 M_\odot$, of which $2800 M_\odot$ is in the extracted region, $r \leq 0.5$. Note from Fig 1 that the narrow density range results in equally narrow ranges of pressure and temperature. Extracting a spherical volume from a larger simulation in this way results in the edge of the volume cutting through some structure, but the range of density and pressure is low enough that this has little effect. The gravitational potential is also smoothly symmetric and relatively shallow. It is against this potential background of the developing cloud complex that deep localised wells should form, if the subsequent clumps in the complex undergo gravitational collapse.

It is also useful to consider the other stable density matching this pressure, specifically $n_H \approx 100 \text{ cm}^{-3}$, as indicated in Fig 2. Assuming isobaric evolution, this is the highest density that can be achieved by thermal instability alone with this choice of heating and cooling techniques and parameters. In reality, the pressure which is roughly the same across the cloud, reduces with time, so this provides a first order estimate in monitoring when gravity begins to be-

**Figure 2.** Equilibrium curves. Thermal equilibrium pressure (P_{eq}/k - thin line) and temperature (T_{eq} - thick line) vs. density for the cooling and heating functions selected in this work. Where the grey dashed line intersects the pressure curve (thin black line) indicates, from left to right, the stable, unstable and stable equilibrium states. Raw data is available from <https://doi.org/10.5518/483>.

come important: densities above this level indicates gravity taking over from the thermal instability.

3 NUMERICAL METHODS AND MODEL

The MG HD code has been used here in the same manner as throughout Papers I to IV. It is an upwind, conservative shock-capturing scheme employing multiple processors through parallelisation with the message passing interface (MPI) library. Integration in time proceeds according to Falle (1991) using a second-order accurate Godunov method (Godunov 1959) with a Kurganov Tadmor (Kurganov & Tadmor 2000) Riemann solver. Self-gravity is computed using a full-approximation multigrid to solve the Poisson equation. The same hierarchical AMR method (Falle 2005; Huber, Falle & Goodwin 2013) is employed on an unstructured grid. Free-flow boundary conditions were imposed on all boundaries. For more details, please consult Papers I to IV and Paper I in particular.

Table 1 presents details of the simulations presented in this work, as well as the Paper IV HD simulation. The HD simulation in Paper IV employed 8 levels of AMR, with

$8 \times 8 \times 8$ cells on the coarsest G0 grid over a domain 300 pc on a side, making the finest grid resolution available 0.29 pc on G7. G0 needed to be coarse to ensure fast convergence of the MG Poisson solver. The central region of this simulation was extracted in order to provide the initial condition for resimulation, in Models 1 to 4 in this paper. The Model 1 simulation herein defined $10 \times 10 \times 10$ cells on the coarsest G0 level and 5 further levels of AMR. Mapping of the region extracted from the Paper IV HD simulation onto the Model 1 simulation was performed in a simple linear fashion over all three coordinate directions for every cell in question. The diffuse structure in this grid was well-resolved (by 10 or more cells) in order to ensure no loss of detail, as can be seen in Fig. 1. As can be seen from Table 1, the Model 1 simulation has approximately the same finest physical resolution as the original HD simulation from Paper IV. As the Model 1 simulation evolved, sharper, higher density features formed. To better resolve these features new simulations with an additional 1 or 2 levels of AMR were started from various times (Models 2 and 3, respectively). The Model 3 simulation would have 1280^3 cells on its finest level if it were fully resolved. A higher resolution Model 4 simulation added a 9th level of AMR to resolve structure at 0.039 pc, but this was only briefly used due to the high computational cost. The simulations were either increased in resolution from an earlier stage, or stopped, when the maximum densities no longer met the Truelove criterion (Truelove et al. 1997). Finally, to examine the final evolution of the most massive clump, an extra Clump resimulation extracted the 0.2^3 region ($10 \times 10 \times 10$ pc) containing this clump and resimulated it at a resolution of 0.016 pc in order to investigate gravitational collapse of this individual clump, details of which are provided on the final line of Table 1. The simulations were typically run across 96 cores of the ARC2-MHD DiRAC1 HPC facility at the University of Leeds (see also the Acknowledgments) and used in excess of 100,000 CPUhours.

3.1 Heating and cooling prescriptions

The same heating and cooling prescriptions from Papers I to IV were employed, which are now summarised in brief. A constant heating factor of $\Gamma = 2 \times 10^{-26} \text{ ergs}^{-1}$ was used, with the heating rate equal to $\Gamma\rho$. For low-temperature cooling ($\leq 10^4$ K), the detailed prescription of Koyama & Inutsuka (2000), fitted by Koyama & Inutsuka (2002), and corrected according to Vázquez-Semadini et al. (2007) was used. At temperatures above 10^4 K the CLOUDY 10.00 prescription of Gnat & Ferland (2012) was used. These choices have enabled the definition of cooling rates over the temperature range from 10 K to 10^8 K - the range required by subsequent feedback simulations. The complete cooling prescription has been efficiently implemented as a lookup table. The neglected processes and simplifications in this approach are discussed at length in Paper I.

It is worth emphasizing here that a different choice of heating and cooling prescriptions can give very different results, in some cases suppressing the unstable region almost entirely (see Wolfire et al. 1995, and their Fig 4 in particular). Micic et al. (2013) studied the influence of the choice of cooling function on the formation of molecular clouds in high-resolution three-dimensional simulations of converging flows. They found that a number of the cloud properties,

such as the mass and volume filling fractions of cold gas, are relatively insensitive to the choice of cooling function. On the other hand, the cloud morphology and the large-scale velocity distribution of the gas do strongly depend on the cooling function. They also investigated the properties of the dense clumps formed within their cloud. They found that the majority of these clumps are not self-gravitating, suggesting that some form of large-scale collapse of the cloud may be required in order to produce gravitationally unstable clumps and hence stars. It remains to be explored in future work the extent to which different heating and cooling prescriptions affect this work. The prescriptions used herein, that study precisely such a large-scale collapse as referred to by Micic et al., are appropriate for the column density of the initial diffuse atomic cloud in our simulations.

4 RESULTING EVOLUTION OF THE CLOUD

The evolution of the cloud and the properties of the structure formed across the cloud complex are discussed in this Section. In particular, time-variation of properties and derived statistics as well as time-snapshots of slices, projections and isosurface plots reveal these properties. Plotting mechanisms within the MG code are used as well as the visualisation software VisIt (VisIt Collaboration 2012).

4.1 The dynamic evolution of the cloud

Fig. 3 provides an overview of the evolution of the cloud, from when the first condensations cause steep density increases at $t=23$ Myrs to the gravitational contraction of the cloud complex as a whole, on a time-scale of the 50 Myr free-fall time. For comparison, the timescale of the maximum growth rate of the thermally unstable initial condition with zero thermal conduction is 5.6 Myrs (as calculated using eq. 31 of Field 1965).

Strikingly evident from this figure is the formation of obvious filaments, existing with high densities over 100 cm^{-3} for more than 10 Myrs. These filaments connect the clumps that are condensing from the unstable medium at the highest density locations. Over time, the clumps grow in size and mass and as the volume of the cloud complex contracts under gravity, effectively absorb the filamentary network that connected them. This is precisely the accepted picture of star formation outlined in the introduction to this paper. Here, this state has evolved naturally from a diffuse stationary initial condition, under only the influence of thermal instability and self-gravity.

Fig. 3 also reveals the long-lasting nature of the filaments - once they have formed, around 25 Myrs into the simulation, they exist for the next 15 Myrs. Measured widths increase over this period as the filaments accrete material, although lengths reduce as the clumps approach one another during the gravitational collapse of the whole cloud. There is no evidence in this hydrodynamic simulation of striation-like structure perpendicular to the filaments. This is in agreement with the fact that striations are thought to arise from the effect of magnetic fields (Tritsis & Tassis 2016). We see such magnetically-aligned striations in our MHD simulations (e.g. as can be seen in fig. 3 of Paper IV) and will explore

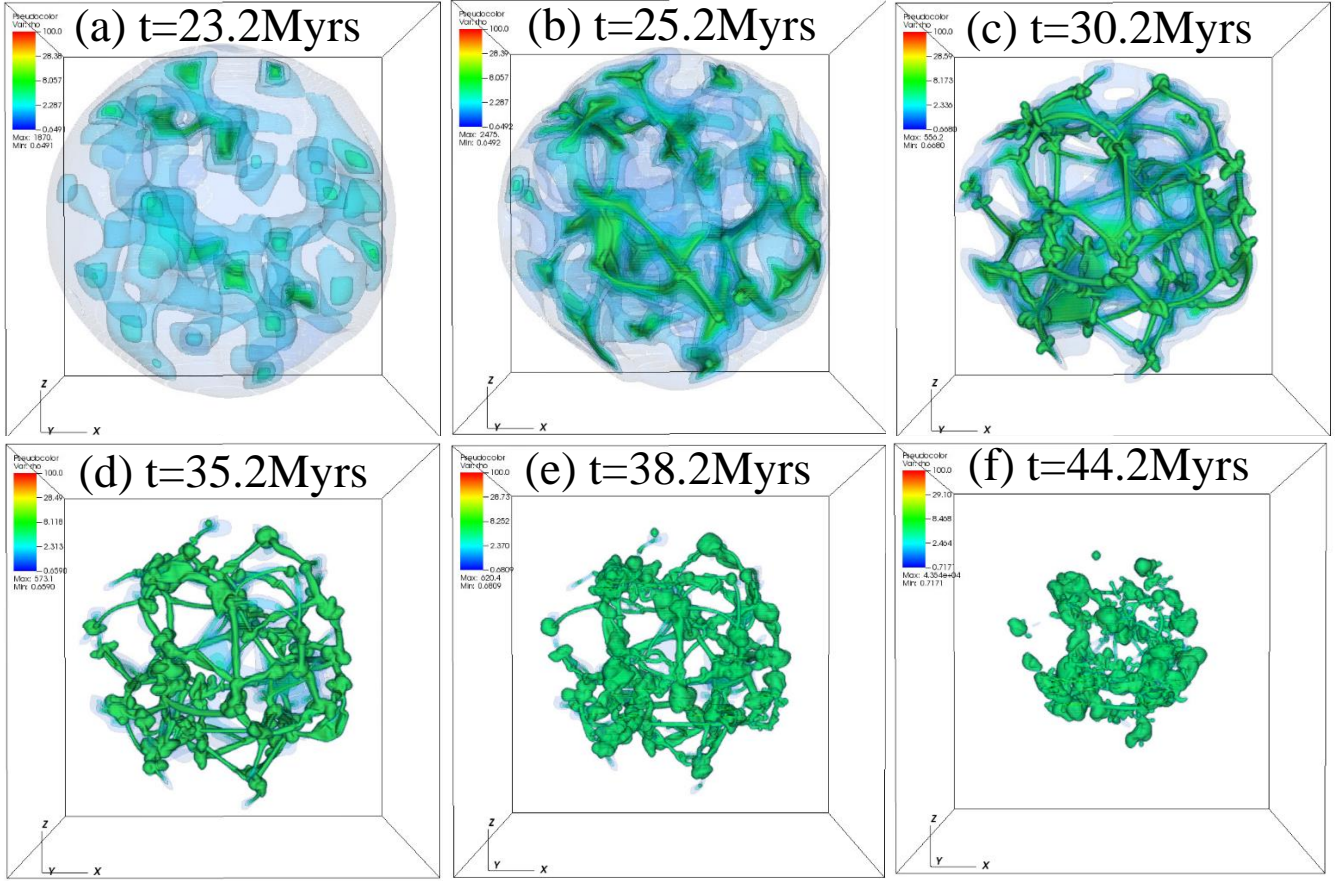


Figure 3. Evolution of the diffuse cloud into a complex of clumps shrinking through gravitational collapse. Six time snapshots from Model 3 are shown, in a box with sides of length 50 pc. Each snapshot shows a 3D isosurface rendering of density, with ten isosurfaces shown at density levels ranging linearly up to $n_{\text{H}}=100 \text{ cm}^{-3}$. Isosurface opacity increases with density, reaching high opacity by $n_{\text{H}}=10 \text{ cm}^{-3}$, sharper and coloured green (digital-only) in the figure. Lower density more translucent isosurfaces are diffuse and bluer in colour (digital-only), indicating the extent of unstable material ($1 < n_{\text{H}} < 10 \text{ cm}^{-3}$). The isosurfaces have been created from Silo datafiles using the VisIt toolkit. Movie and Silo format raw data files are available from <https://doi.org/10.5518/483>.

their origins in the follow-on equivalent magnetic paper (in prep.) to this hydrodynamic paper.

The filamentary nature of the cloud in this hydrodynamic simulation came as somewhat of a surprise. Our previous work (Wareing et al. 2016) had revealed filamentary structure in projection of MHD simulations, but no clear indications of filaments in any of the purely HD simulations. That previous work had a base level resolution of 0.29 pc, at least four times lower than that shown in Fig. 3 and comparable to the largest filamentary widths measured from Model 3. Any filaments in earlier HD work should have been at the very limit of detection. Even so, reexamination of the hydrodynamic simulations presented in Paper I reveals that early in their evolution, the numerous clumps forming across the cloud have a tendency to be elongated toward each other. Isosurface rendering has shown this nature more clearly than column density projections shown in Paper I, which are uniformly clumpy. The existence of elongated structure, even at the grid-scale in these early simulations, lends credibility to their convincing detection at the higher resolutions employed here.

It is now prudent to investigate these filaments further. In Figure 4 we show slices and cuts through the domain that

illustrate the structure and flow in a long-lived filament. It is clear from comparing planes at $z = 0$ to perpendicular planes at $y = 0.1$ that these structures are indeed extended linear filaments, several pc long compared to their sub-pc widths. The spacing between the high density regions is 5–10 pc, which is of the order of the acoustic length scale, defined as the sound speed multiplied by the cooling time. These regions then evolve into the filaments and clumps as the thermal instability develops. Unstable gas flows onto the filament and over time they grow in width, from 0.26 pc at 30.2 Myrs to 0.56 pc at 36.2 Myrs in the filament shown here (FWHM measurements of the density peaks in (e) and (f)). The radius is not a property of the thermal instability, but instead is defined by the amount of unstable gas that can fall in due to the flow induced by the thermal instability. All the same, these widths are in reasonable agreement with the observed range of filamentary widths (Panopoulou et al. 2017) and the debated characteristic width of filaments (Arzoumanian et al. 2018), especially bearing in mind the difference between the density peaks measured here and observational measurements based on molecular emission. It is worth repeating here that the resolution of the simulation presented in Fig. 3 is 0.079 pc. The Model 4 simulation goes

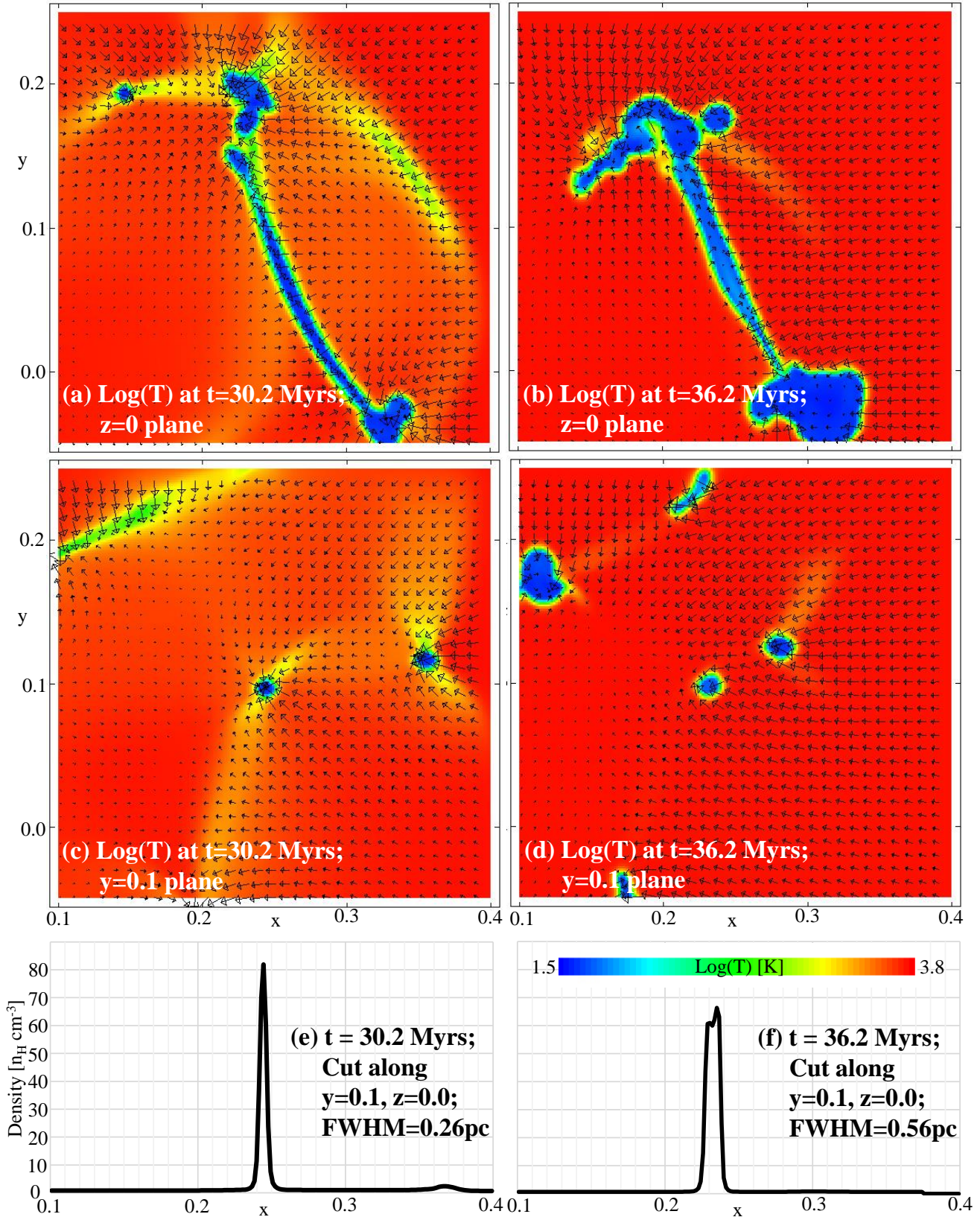


Figure 4. Detail of a particular filament and its appearance at 30.2Myrs and 36.2Myrs. (a) and (b) show slices of temperature on the $z = 0$ plane revealing flow onto and along the filament at 30.2 and 36.2Myrs respectively. (c) and (d) show slices of temperature perpendicular to this on the $y = 0.1$ plane at the same times revealing flow towards the filament and its short extent in the x and z directions compared to the elongation shown in (a) and (b). (e) and (f) show cuts in density along $y = 0.1, z = 0$ revealing the sharply peaked nature of the filament and its width. Raw data is available from <https://doi.org/10.5518/483>.

down to 0.039 pc in high resolution studies of this period of the cloud evolution. The grid resolution is considerably less than the measured width of the filaments in the simulation - they are not forming on the grid scale of these simulations.

Velocity vectors on the planes in (a) to (d) illustrate the nature of the flow. The flow onto the filaments from the surrounding medium is clear, with velocities on the order of a few km s^{-1} , but careful inspection of the velocity vectors inside the filament shown in (a) and (b) reveals flow along the filaments at magnitudes of less than 1 km s^{-1} towards the growing clumps at either end. This is in good agreement with observations (Peretto et al. 2013). Further work is now planned to explore the mass-flux onto and along these filaments and the difference introduced by magnetic fields of various strengths.

During the early evolution of the cloud, the over-dense regions present in Fig. 1 increase in density, and then briefly stretch into sheets before becoming filaments, whilst a clump grows at their centre. Examination of the pressure distribution in Fig. 1 illuminates some reasons for this evolution. In the unstable range, regions of higher density have lower pressure, hence the flow of material from high to low pressure increases the density further and pushes the region into cold stable phase. Reducing density at the high pressure locations, as a consequence of material flowing away from these regions, stabilises tenuous low-density warm material. This is analogous to the formation of a foam under phase transition, where the condensed liquid exists in an interconnected filamentary network with bubbles of gas - bench-top X-ray tomography of a monodispersed liquid foam has revealed a strikingly similar structure (Meagher et al. 2011) to that which is produced here and shown in Fig. 3. There are also similarities to Voronoi foam, which has been applied at cosmological scales to models of galaxy distributions (see, for example, Icke & van de Weygaert 1991, and references to this work).

4.2 Evolving properties of the cloud

Fig. 5(a) gives mass in the appropriate temperature range, which does not mean that it is on the equilibrium curve, for a subset of the time evolution. The first 15 Myrs of the evolution are not shown as nothing varies. The filamentary network that develops is characteristic of the transitional phase as the simulation evolves the unstable diffuse material into stable states. As the majority of the mass stabilises into either warm or cold states, the filaments are absorbed into the individual cold clumps of the collapsing cloud complex. These individual clumps have much higher densities and hence have the potential to collapse under gravity and form stars on shorter timescales than the whole cloud complex.

The mass distribution of cloud material at $t=44$ Myrs in the Model 3 simulation is shown in Fig. 5(b). It is clear from this plot that material still persists out of equilibrium in the unstable density range. Analysis of the mass distribution of material by density range reveals that approximately 10% of the cloud material is in the density range from 1 to 10 cm^{-3} (c.f. for the Paper IV HD simulation, the fraction is approximately 35% at $t=36$ Myrs - considerably more than the fraction of 5% implied from Fig. 5(a) at this time). As this material is out of equilibrium, it is difficult to

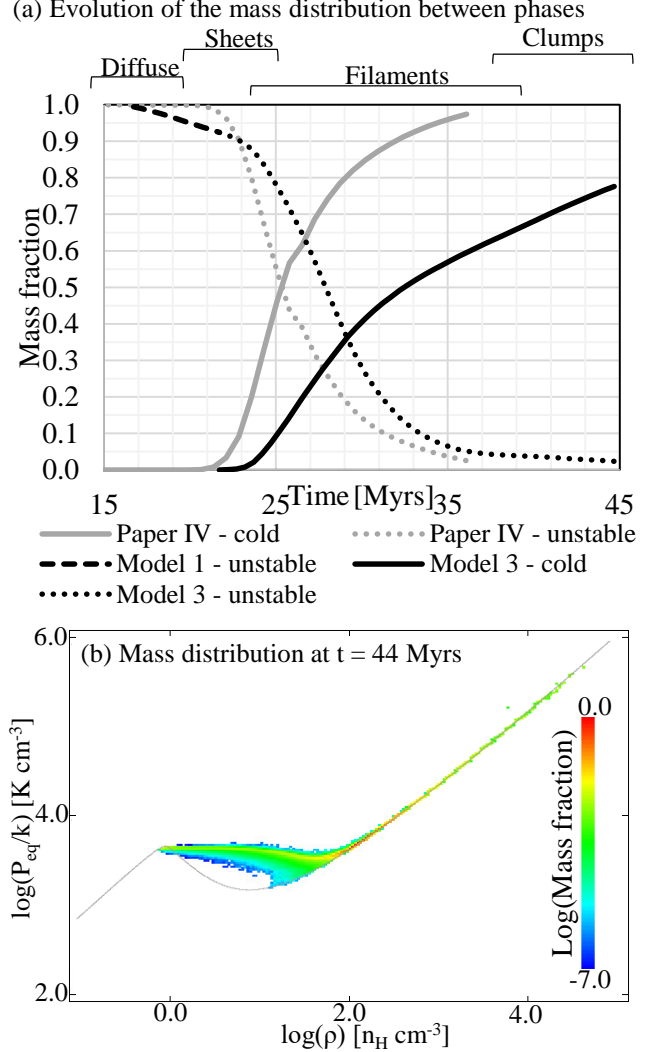


Figure 5. (a) Evolution of the mass in the appropriate temperature range (cold $< 160 \text{ K}$, $160 \text{ K} < \text{unstable} < 5000 \text{ K}$, warm $> 5000 \text{ K}$), with indications of the dominant structure at that time above the line graph. (b) Mass distribution of the cloud material in the Model 3 simulation at $t=44.2$ Myrs, as shown in Figure 3(f). The grey line indicates the equilibrium curve for our choice of heating and cooling prescriptions. Raw data is available from <https://doi.org/10.5518/483>.

classify and nominally should be assigned to its final state, as we have done here using ranges in temperature. Hence, the mass fraction of unstable material in equilibrium is low, as shown in Fig. 5(a), but the volume-filling-fraction of this low-density non-equilibrium material is comparatively high. Observations have confirmed that such thermally unstable material can be detected in the temperature range 400 to 900 K (Begum et al. 2010). Whilst the model herein is clearly able to dynamically produce thermally unstable gas, further work is required to compare this in detail to observations. Fig. 5(b) also shows the high density material at high pressure in thermal equilibrium, now collapsing under gravity in the individual cold dense clumps of the complex.

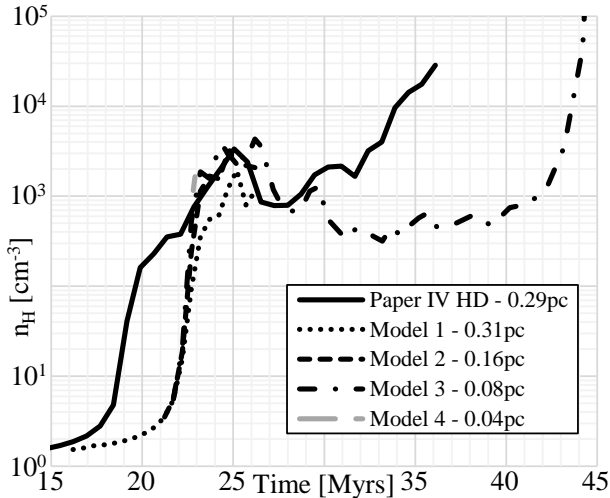


Figure 6. Evolution of the maximum density in the domain. The faster formation of dense clumps in the Paper IV HD simulations is due to the compression at the outer surface of the cloud, which results from our choice of initial conditions (see main text). Raw data is available from <https://doi.org/10.5518/483>.

The variation of maximum density with time is shown in Fig 6, for the same subset of the time evolution. The time indicated on the horizontal axis is that elapsed since the start of the Paper IV HD simulation; the first 15 Myrs are similarly not shown as the maximum density is close to the initial density in the diffuse atomic cloud. The black solid line indicates the trend of maximum density from the Paper IV HD simulation. The steep rise from 18 to 21 Myrs is due to condensations close to the edge of the cloud that have been influenced by the pressure difference caused by the reducing average pressure across the cloud compared to that of the surrounding medium. Whilst these may or may not be representative of reality, in this work the study of thermal instability and gravity is under examination, hence the isolation of the central region of the Paper IV HD cloud extracted and used to define the initial condition of the Model 1 simulations. This is also the reason for the *reduction* in the maximum density present in the domain at the initialisation of the Model 1 simulation and the steep rise in density shown after 30 Myrs by the Paper IV HD simulation, which is the gravitational collapse of the condensations close to the edge of the cloud.

The maximum densities in the Model 1-4 simulations are representative of structure solely generated from the thermal instability. These simulations show that thermal instability triggers a steep rise in density around 22 Myrs, as the filamentary network forms. During this steep rise, at 21.7 Myrs the Model 2 and Model 3 simulations are both started by adding extra levels of AMR in order to ensure resolution of later structure; the starting of simulations with extra levels of AMR is earlier than the maximum density peaks as adding extra levels of AMR once already at peak density risks loss of unresolved structure in the run up to that time.

By 23 Myrs, the maximum density in the Paper IV HD simulation is back in agreement with the maximum densities present in the Model 1, 2 and 3 simulations. The maximum density in the Paper IV simulation is now representative of

thermal instability-driven structure in the extracted central $r=0.5$ (25 pc) region of the cloud used to initialise the Model 1 simulation, rather than condensations close to $r=1.0$ that were unduly influenced by the pressure difference between cloud and surroundings. These condensations lead to the marked difference between the Paper IV HD simulation and all the other simulations in Fig. 6.

By 25 Myrs, the maximum density in all simulations is in agreement and reaches $n_H \approx 3000 \text{ cm}^{-3}$. A detailed inspection of this behaviour (through adding an extra level of AMR at $t=22.8$ Myrs to initialise the Model 4 simulation) indicated that it *does not* lead to gravitationally bound clumps that may subsequently form stars. Inspection of the velocity field around these structures reveals velocities on the order of a few km s^{-1} that are non-convergent, resulting from flow of thermally-stable material from warm, tenuous to cold, dense conditions. Kinetic energy dominates and as a result, these structures break apart on relatively short timescales compared to their free-fall times. The long duration of the relatively high maximum density in Fig 6 from 24 to 27 Myrs is indicative of the period over which the filamentary structures form and evolve in the cloud. It is not the peak density of individual clumps that may collapse under the effect of gravity. The Model 3 simulation resolves the peak in maximum densities into several separate peaks for this reason.

The importance of correctly identifying this period of dynamically-dominated structure in any simulations cannot be over-emphasized. Dynamical and non-equilibrium effects have been shown to be important for cloud evolution (Goicoechea et al. 2016). Mechanisms for forming star particles could mis-identify these regions of high density, as they meet conditions for inward flow, potential minimum and Jeans instability. Depending on the frame of reference selected for calculating energies, the balance between kinetic, gravitational and thermal energy can also be misleading, an issue that has also been noted in observations (Ballesteros-Parades et al. 2018). Followed carefully at high resolution, they do not collapse under their own self-gravity.

The original Paper IV HD simulation contained sharp unresolved structures at this time and did not resolve multiple dynamic peaks around 25 Myrs, but did capture the transience of this period, reducing back to lower densities in the cloud until the condensations at the edge of the cloud begin to collapse around 29 Myrs. The resolved Model 3 simulation captures the true collapse of quiescent thermal instability-driven structure beyond this point showing that longer-lasting filamentary structure forms with densities on the order of several hundred per cubic centimetre. By 40 Myrs or so individual clumps have gathered enough mass to begin to collapse under the influence of gravity. This is against the background of the infall towards the deep central potential well at the centre of the domain. There is therefore a long period of time (up to 10 Myrs from $t=28$ Myrs) where the cloud consists of quiescent high density clumps connected by lower density filaments that have not collapsed under gravity. These clumps have size scales on the order of a few pc and are therefore not diffuse microstructure in the ISM (Stanimirović & Zweibel 2018), but do resemble pressure confined clumps noted as a pre-requisite for star formation (Kainulainen et al. 2011). Whilst we do not track the formation of molecules, the timescale here is not dissimilar to the ~ 10 Myr time scale of cloud formation recently

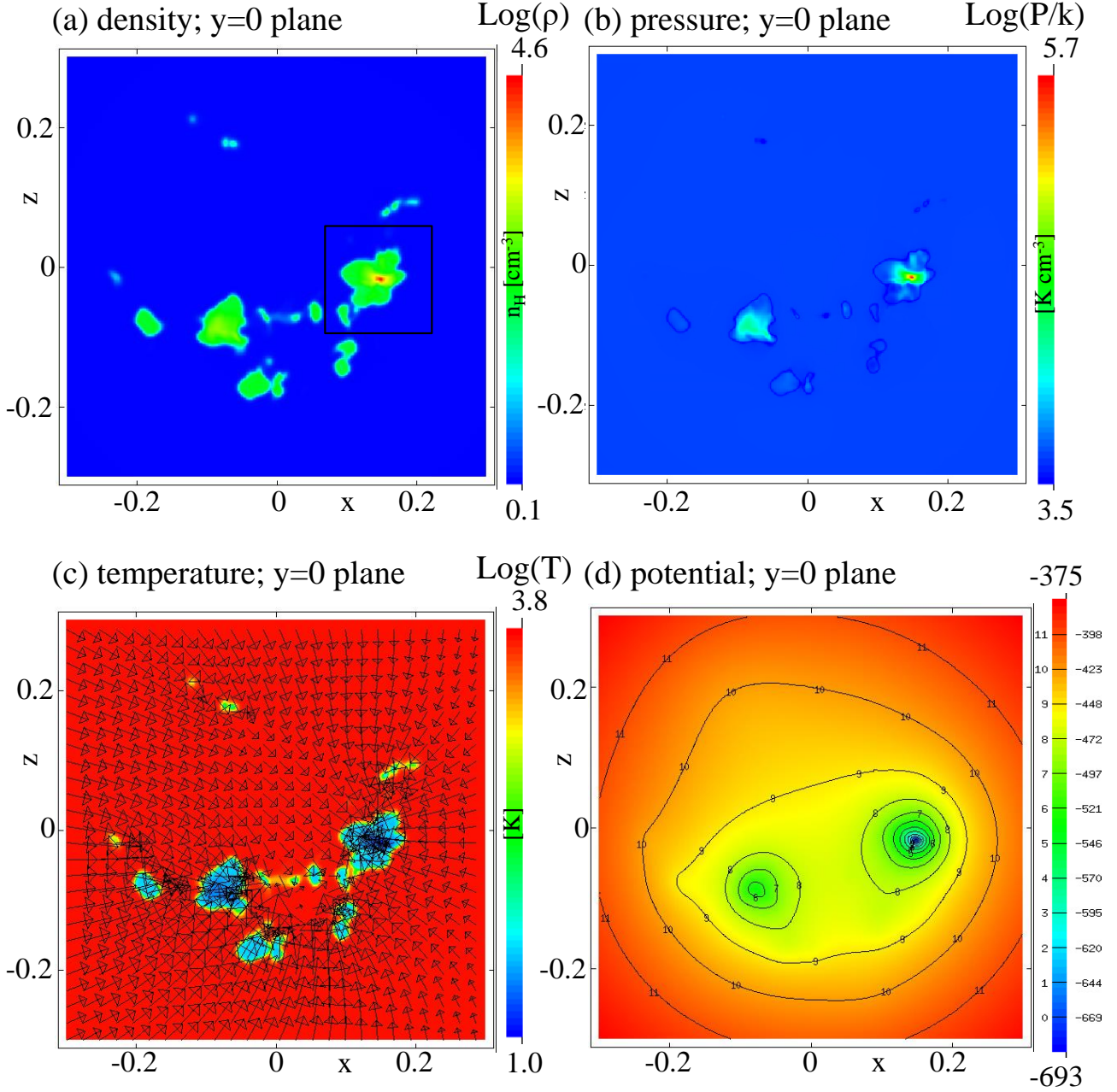


Figure 7. The evolved simulation, showing a slice through the domain at $y=0.11328$ through the densest clump in the grid. Shown are (a) density, (b) pressure, (c) temperature and (d) gravitational potential of the Model 3 simulation at $t=44$ Myr. Vectors of velocity, scaled on the largest magnitude in the slice of 2.5 km s^{-1} , are shown in panel (c). The box in panel (a) indicates the volume, centred on the most massive clump, resimulated later at higher resolution. The unit of distance is 50 pc. Raw data is available from <https://doi.org/10.5518/483>.

derived for formation of molecular hydrogen in an isolated dark cloud (Zuo et al. 2018).

5 AN INVESTIGATION OF THE CLOUD AT $T=44$ MYRS

The appearance of the cloud as a whole at $t=44$ Myrs is shown in Figs. 7 and 8. This is the time at which the majority of the material in equilibrium in the domain has stabilised and can be considered the thermal end-state of the

cloud. The remaining unstable material is in thin layers surrounding the clumps. Few filaments remain. In the unrealistic scenario that stars do not form, the future of the cloud is collapse under gravity on the free-fall timescale of the cloud. The question is whether individual clumps can or are collapsing on shorter time scales. Slices of density, pressure, temperature and potential through the simulation domain show the clumpy nature of the cloud complex, as well as the fact that only the most massive clumps have increased central pressures at this time. The temperature slice shows both temperature on the colour scale and vectors of total ve-

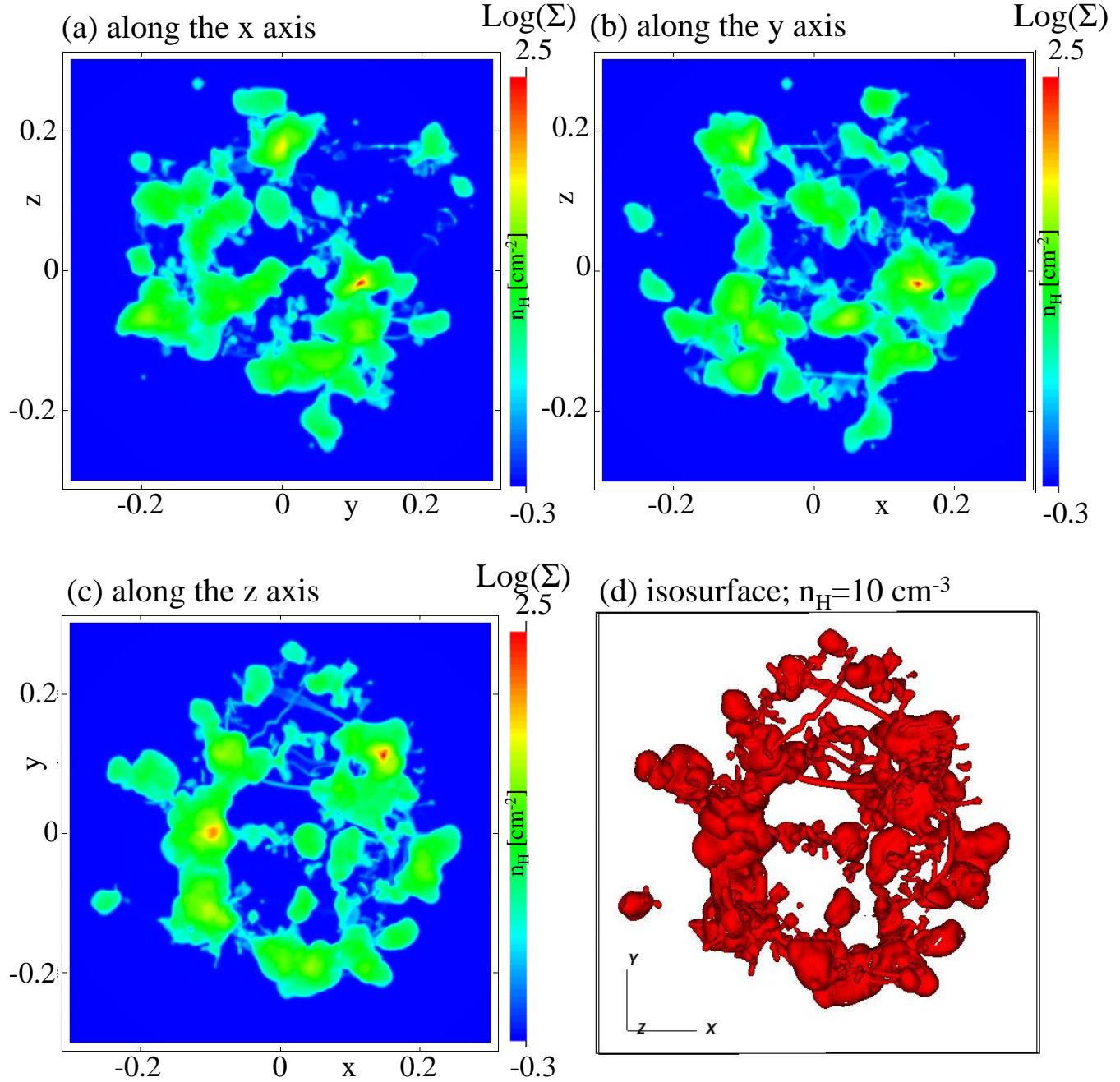


Figure 8. Projections of column density in the three axial directions and an isosurface of density, rotated to match the projection along the z axis for side-by-side comparison, of the Model 3 simulation at $t=44$ Myrs as in the previous figures. The unit of distance is 50 pc. Raw data is available from <https://doi.org/10.5518/483>.

locity projected onto this plane. The uniformity of the warm stable surroundings is immediately apparent - there is effectively very little variation across this intra-clump medium, even though the flow field is complex. The velocity vectors show there are inflows towards the individual clumps apparent on this plane, as well as the overall infall towards the centre of the most massive clump. The depth of the potential well, as well as the previously noted smooth nature of the distribution is apparent from the slice through potential. These slices through the domain do not show any filamentary structures. At this time, they are now rare, having

been absorbed into clumps, or dissipated along their length into chains of smaller clumps. Fig. 8 shows projections of column density in the three axial directions and a density isosurface of the Model 3 simulation, revealing the few remaining filaments. In particular, in the upper right of panel (a), the break-up of a filament into a series of clumps along its length appears to be occurring at this late time.

Table 2. Properties of the 21 clumps with more than $20 M_{\odot}$ identified by the FellWalker algorithm, at $t=44$ Myr in the Model 3 simulation. Snapshots of slices through the clumps are available from <https://doi.org/10.5518/483>.

	M_{total} [M_{\odot}]	M_{warm} [M_{\odot}]	$M_{unstable}$ [M_{\odot}]	M_{cold} [M_{\odot}]	ρ_{max} n_H [cm^{-3}]	T_{min} [K]	Scale [pc]	v_{max} [km s^{-1}]	v_{min} [km s^{-1}]	Notes
A	2.37e2	5.39e1	3.19e0	1.78e2	4.62e2	30.5	3.5	2.2	0.11	Spheroidal, extended arms
B	2.64e2	2.36e1	4.10e0	2.37e2	9.92e2	21.5	4.0	2.8	0.31	Prolate spheroid
C	2.71e2	4.49e1	4.25e0	2.22e2	7.76e2	22.9	4.0	2.4	0.12	Pyramidal
D	3.54e2	5.65e1	6.49e0	2.92e2	1.46e4	10.6	4.0	2.5	0.17	Multiple lobes
E	7.27e1	1.05e1	1.01e0	6.12e1	4.16e2	31.3	2.5	1.9	0.03	Spheroidal
F	1.08e2	1.55e1	1.01e0	9.12e1	4.32e2	28.8	4.0	2.6	0.06	Double sphere merger
G	1.77e2	1.94e1	2.65e0	1.55e2	3.31e2	32.7	4.0	2.1	0.04	Peanut
H	2.65e1	2.01e0	3.19e-1	2.42e1	1.54e2	32.4	2.4	2.5	0.03	Clump on a filament?
I	7.57e1	5.88e0	1.06e0	6.88e1	1.94e2	33.4	3.0	2.2	0.18	Results of a merger?
J	3.13e1	2.59e0	2.93e-1	2.84e1	2.16e2	32.0	3.0	3.2	0.08	Co-flowing clumps
K	1.04e2	5.10e0	1.14e0	9.76e1	4.18e2	26.9	2.5	1.8	0.03	Isolated. Spherical
L	2.37e1	1.02e0	3.28e-1	2.23e1	2.83e2	31.1	1.0	2.5	0.01	Tadpole, 2.5 pc elongated tail
M	6.83e1	1.16e1	1.07e0	5.57e1	4.95e2	26.1	3.0	2.7	0.03	Elongated. Chain?
N	9.14e1	8.50e0	1.42e0	8.15e1	3.33e2	29.3	3.0	2.4	0.33	Spheroidal, linked filament?
O	4.85e1	8.63e0	1.28e0	3.87e1	2.34e2	29.9	3.0	1.7	0.02	Spheroidal - 2 filaments
P	6.84e1	2.20e1	1.66e0	4.47e1	1.89e2	33.1	3.0	1.9	0.07	Large tadpole
Q	6.63e1	5.19e0	9.80e-1	6.01e1	2.86e2	32.1	4.0	1.8	0.03	Sph. Off-centre max rho
R	2.96e2	3.19e1	2.76e0	2.62e2	3.25e3	16.9	5.0	2.4	0.13	Multiple lobes - subclumps?
S	7.25e1	7.70e0	1.00e0	6.38e1	3.92e2	27.4	5.0	2.5	0.02	Double merger
T	3.57e1	1.53e0	7.64e-1	3.34e1	2.06e2	33.0	3.0	2.3	0.03	Prolate spheroid
U	3.36e1	3.72e-1	3.91e-1	3.28e1	2.03e2	33.6	2.5	2.7	0.15	Spheroidal, sub-clumps

5.1 Analysis of the clumps across the cloud

It is now meaningful to identify and analyse massive clumps in the simulation. The FellWalker clump identification algorithm (Berry 2015) has been implemented into MG in order to do this. Berry described FellWalker as a watershed algorithm that segments multi-dimensional data above a pre-set background level into a set of disjoint clumps, each containing a significant peak. It is equivalent in purpose to the CLUMPFIND algorithm (Williams, de Geus & Blitz 1994), but unlike CLUMPFIND, FellWalker is based on a gradient-tracing scheme which uses *all* the available data, ‘walking’ from each datapoint according to the steepest gradient to the peak associated with that gradient. Berry performed comparisons with CLUMPFIND and showed that the results produced by FellWalker are less dependent on specific parameter settings than are those of CLUMPFIND.

Whilst Berry designed FellWalker to identify significant peaks in density, here FellWalker has been implemented to identify significant wells in gravitational potential. The gravitational potential has a significantly smoother distribution than the mass distribution and hence makes an excellent choice for identifying clumps directly from the simulation without any parameterised smoothing step. After implementation, the algorithm was thoroughly tested with simple 2- and 3-dimensional potential distributions to establish confidence in the performance and understand the optimum grid configuration for usage. In order to achieve the best results, we applied FellWalker to the potential projected onto the finest grid level. The potential is sufficiently smooth for the projection from coarser grids to be smooth enough for FellWalker.

Applying FellWalker to the Model 3 simulation snapshot at $t=44$ Myrs, the algorithm detects 21 individual clumps with masses greater than $20 M_{\odot}$. This particular time is the time at which the highest density in the sim-

ulation, in the centre of the most massive clump, reaches the limit of the resolution. It should be noted that this most massive clump is not at the centre of the simulation. The term ‘clump’ is used by choice in order to achieve clarity from the diffuse initial cloud condition and the cloud complex that the combination of these clumps forms. Bergin & Tafalla (2007) review the properties of clumps based on Loren (1989) and Williams, de Geus & Blitz (1994): mass $50\text{--}500 M_{\odot}$; size $0.3\text{--}3$ pc; mean density $10^3\text{--}10^4 \text{ cm}^{-3}$, velocity extent $0.3\text{--}3 \text{ km s}^{-1}$; sound crossing time 1 Myr; and, gas temperature $10\text{--}20$ K. Properties of the 21 massive clumps identified in the Model 3 simulation are shown in Table 2. The range of mass, maximum density, size scale and velocity fit the description of Bergin & Tafalla very well. In each clump, the majority ($> 75\%$) of the mass is in the cold phase. Minimum temperatures, which occur in the inner regions of each clump where the lowest velocity also occurs, are typically slightly higher than Bergin & Tafalla’s review; only the two most massive clumps, D and R, are colder than 20 K in their core. It is worth noting that maximum density and minima of temperature and velocity are all co-located in these cold (< 100 K) inner regions of each clump, but often not at the centre of mass of the clump, reflecting the complex evolution that has produced these clumps.

The maximum velocity is usually found at the edge of the clump, which is well-defined by a sharp gradient in temperature. Material there is falling into the clump whilst rapidly cooling and decelerating through the phase change - these are dynamic rather than stationary accreting objects. They are not simply cold clumps stabilising out of quiescent unstable surroundings. The surroundings are in fact in the warm stable phase and the only unstable region is across the sharply defined edge of the clump, hence the “unstable” mass (defined as that in the unstable region of Fig 2, with densities between $n_H=1.0$ and 10.0 cm^{-3}) is a small fraction of the total clump mass.

The appearance of the clumps is varied, as noted in Table 2. Very few are isolated and spherical, reflective of the fact that they have absorbed filaments and smaller clumps. What Table 2 only partially alludes to, is the remnants of filamentary interconnecting structures between clumps. This is present at $t=44$ Myrs as smaller condensations where a filament has dissipated along its length, extended wings stretching away from the clumps where filaments are being absorbed and the existence of isolated small clump-like structures. These small structures have masses on the order of a few solar masses or less and have shallow potential wells, if any discernible effect on the gravitational potential. In time, the isolated small structures may grow, or merge into existing clumps, as all are falling toward the centre of the cloud complex. At this time in the Model 3 simulation, there are no discernible sheet-like cloud collisions. The subsonic velocities in the simulations here do not lead to shock-compressed thin structures.

The maximum and minimum velocities in Table 2 are not reflective of the velocity dispersion of the individual clumps. The maximum velocity reflects the typical velocity of the infalling material at the edge of the clump, uncorrected for the velocity of the centre of the mass of the clump falling towards the centre of the cloud complex, up to 0.5 km s^{-1} . Further analysis has shown that the minimum velocity is typical of the velocity dispersion of the cold material in the clump, on the order of $0.2\text{--}0.5 \text{ km s}^{-1}$ or less. At the edges of the clump, the velocity of the infalling material is subsonic in the warm stable medium, and approaches Mach number of 1 as the material flows across the temperature gradient at the boundary of the clump. This would appear to be in-line with observations of sonic velocities around clumps, which must dissipate for the clump to eventually collapse under the effect of gravity, converting kinetic energy into thermal and gravitational energy - the potential well deepens whilst the pressure at the centre of the clump rises. The clumps in Table 2 display clear evidence of the relationship between increasing density and deepening individual potential wells, even set against the background of the potential of the cloud complex as a whole. Interestingly, on the smaller scale of cores, Ballesteros-Parades et al. (2018) find the extension of this from clumps to cores - the observed energy budget of cores in recent surveys is consistent with their non-thermal motions being driven by their self-gravity and in the process of dynamical collapse. Furthermore, Micic et al. (2013) study the influence of cooling functions on the formation of molecular clouds and find, in agreement with previous models, that the majority of clumps are not self-gravitating, suggesting that some large-scale collapse of the cloud may be required in order to produce gravitationally unstable clumps and hence stars. We see that effect here and now go on to study an individual clump in detail, followed by study of the final collapse of the most massive clump identified in Table 2.

5.2 Study of an individual clump

Turning to examine an individual clump in more detail, Figure 9 shows slices and profile cuts through Clump R, the second most massive clump in the Model 3 Simulation at $t=44$ Myrs. The slices and profiles are cut through the position of the deepest potential of the clump, at $(-0.0977,$

$0.00078, 0.174)$. The centre of mass of the clump is slightly offset at $(-0.103, 0.00209, 0.181)$, equivalent to 0.44 pc between centre of potential and centre of mass - further reflecting the non-symmetric, non-spherical nature of this clump, 5 pc in length along its major axis. The cut along x reveals multiple peaks in density, with corresponding complex velocity structure, due to the absorption of the filamentary network and merger with other clumps.

It is interesting at this point to compare the density distribution to previous assumptions about clumps. Clearly the clump does not have a uniform density distribution. It does, around the central peak, have a Plummer-like density distribution, indicated in the figure by the agreement between the data (black line) and theoretical profile (grey line). In the negative x direction, this agreement stretches over two orders of magnitude in density - on a linear y -axis scale, the agreement appears very close. The comparison here is with the classic Plummer-like profile introduced by Whitworth & Ward-Thompson (2001), with the observationally confined power-law index of 4, rather than the true Plummer sphere with index of 5. The fit takes a central density of $n_{\text{H}} = 3780 \text{ cm}^{-3}$ from the data and a minimal central flat radius of 0.01 ($\approx 0.5 \text{ pc}$). The temperature plot serves to illustrate the sharply defined edge of the clump, where the temperature ranges quickly from the lower inner temperatures below 100 K , to the high temperature ($> 5000 \text{ K}$) of the warm stable surroundings. Peaks in the inner temperature profiles revealed by the x cut, which correspond to troughs in density, again show evidence for merger with earlier structure in the cloud.

The distribution of the potential, shown in panel (c) of Fig 9 is remarkable for its smoothness compared to the complex structure apparent in density. In the context of simulated molecular clouds, gravitational potential is clearly useful for identification of distinct clumps with structure-finding tools such as FellWalker or CLUMPFIND.

The Mach number of the flow is shown in Fig. 9(d), with vectors indicating the magnitude and direction of velocity, projected onto this plane in Fig. 9(b). Whilst some information is lost in this projection, panel (b) makes it apparent that the highest density, coldest regions of the clump correspond to the lowest velocities inside the clump. The complexity of the velocity field is apparent in Fig. 9(d), indicating accelerating but still sub-sonic inflow from above the clump. Note that velocity on this slice is presented in the frame of reference of the entire simulation domain, rather than corrected for the motion of the centre of mass of the clump towards the centre of the slowly collapsing cloud complex. The velocity of the centre of mass of the clump is approximately 0.5 km s^{-1} towards the lower right corner of the panels, indicated by the uniform velocity field in cold regions of the clump. Clearly, velocity in the frame of the clump reduces as material flows, under the action of the thermal instability, across the phase boundary from warm tenuous to cold dense material. In turn, the dispersion of velocity reduces across this boundary. Adjusting for the motion of the clump, the apparently supersonic regions inside the clump in Fig. 9(d) are in fact subsonic. However, the supersonic material falling into the filament from the warm medium at the righthand edge of the plots is supersonic once inside the cold regions of the filament, indicative of mildly supersonic velocities in filaments.

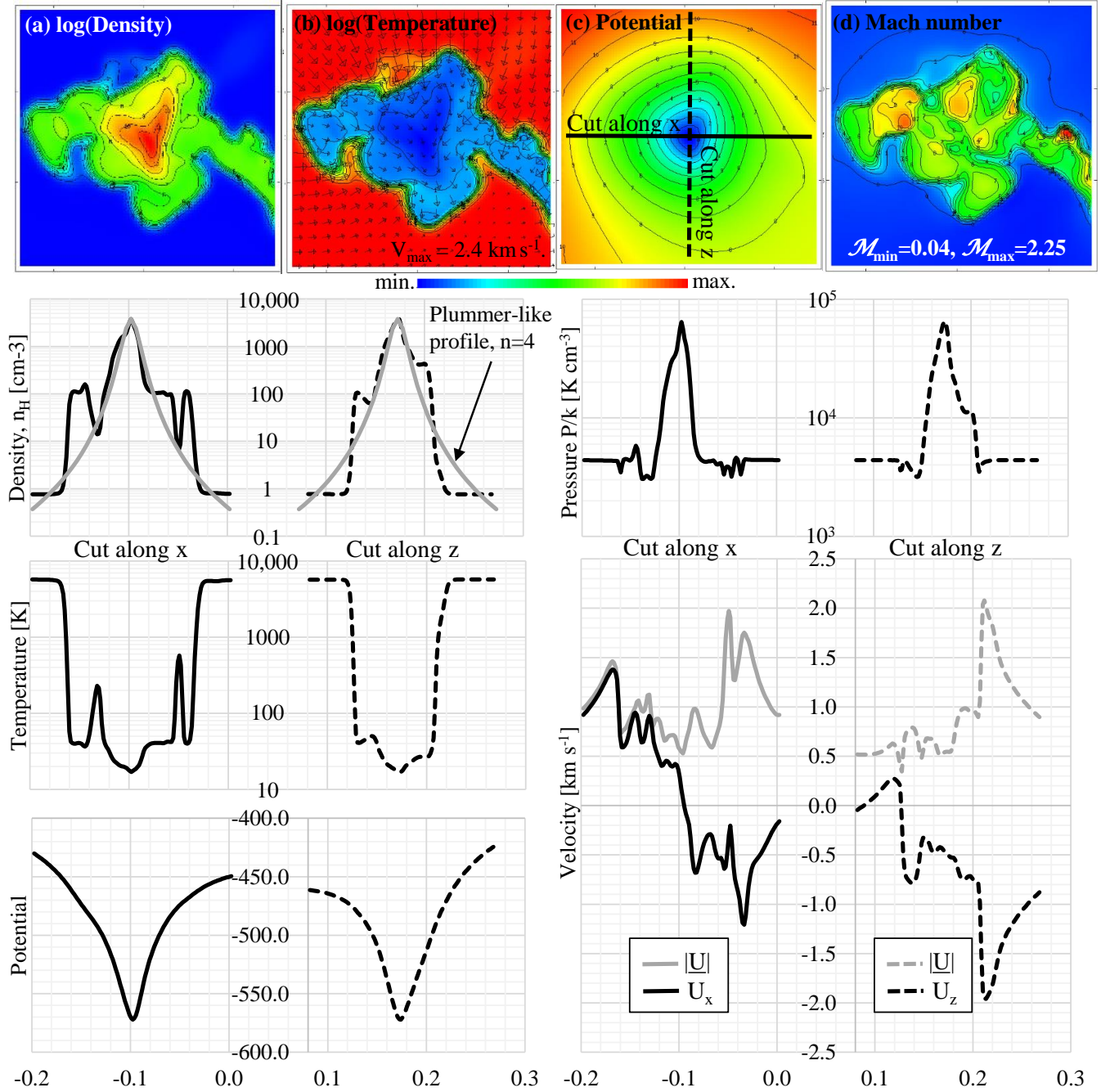


Figure 9. Properties of Clump R from the Model 3 simulation at $t=44$ Myr. The unit of distance is 50 pc. Raw data is available from <https://doi.org/10.5518/483>.

Of key importance in Fig. 9 are the cuts through pressure across the clump. The central pressure is an order of magnitude greater than the equilibrium pressure in the warm surroundings, clearly indicating gravitational collapse. The conditions are close to thermal equilibrium, with pressure at the centre a few percent higher than the corresponding thermal equilibrium pressure for that density. The central density is not in dynamical equilibrium and is still rising as the clump continues to collapse. On the outer edges of the clump are rises in density and small rises in pressure, together with variations in temperature that are indicative of

the merger of clumps and absorption of filaments. The velocities in these regions, in the frame of the clump, are sub-sonic and so there are no shocks present inside the clump.

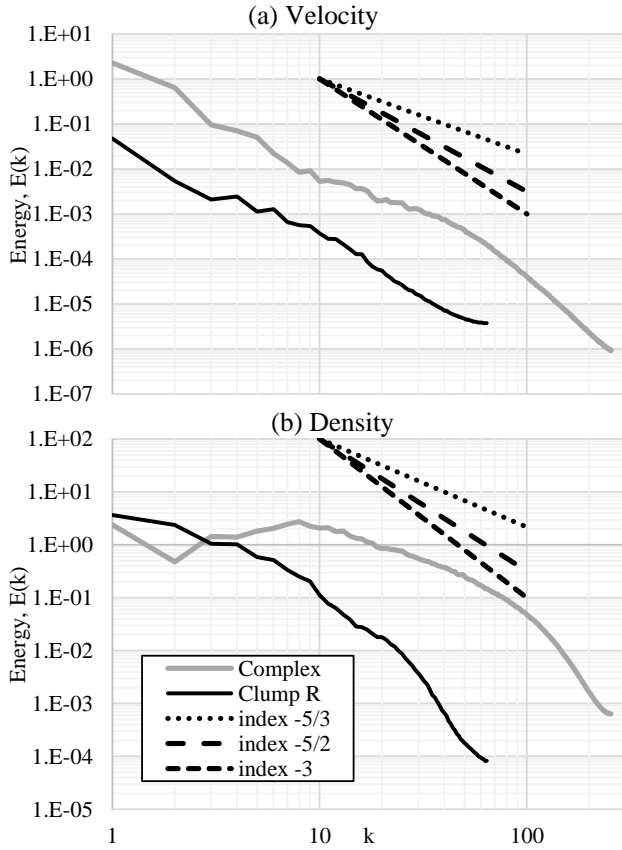


Figure 10. Instantaneous power spectra of a) velocity and b) density for the cloud as a whole and for clump R at $t=44$ Myrs. Raw data is available from <https://doi.org/10.5518/483>.

6 POWER SPECTRA OF THE CLOUD COMPLEX AND AN INDIVIDUAL CLUMP

In Fig. 10 we show the snapshot power spectra of velocity and density both for the cloud complex as a whole and for Clump R at $t=44$ Myrs. The power spectra have been calculated from the magnitude of the complete velocity vector (v_x , v_y , v_z) and the density. There is no projection or smoothing of the velocity vector into two components on a plane (as has been shown to affect velocity power spectra by Medina et al. 2014). Power spectra have been calculated using a simple IDL¹ routine which performs the Fourier Transform and bins the square of the 3D transform into wavenumbers to obtain the 1D power spectra. The validity of this method has been checked by generating density structures in 1D, 2D and 3D. These structures have been generated using single wavenumber sine waves with varying wavenumbers and combinations of these sine waves with multiple component wavenumbers to ensure the power spectra analysis returns the correct wavenumber(s) that was(were) used to generate the density structure in the first place.

Clear from the power spectra of velocity is that both the cloud complex and Clump R display an inertial range (region in wavenumber with slope of constant gradient) greater

than one order of magnitude. The cube encompassing the cloud complex transformed for this analysis was 40 pc on a side. Between wavenumbers 3 and 30 (or physical scales from 13 pc down to 1 pc), the spectral index is close to the Kolmogorov $-5/3$ spectrum generally observed in turbulence. This is in good agreement with observationally-derived velocity power spectra, for example an index of -1.81 ± 0.10 derived by Padoan et al. (2006) for the Perseus molecular cloud complex. At $k = 30$ there is a break in the spectrum, to an index steeper (less than) than -3 implying rapidly reducing kinetic energy with decreasing physical size scale. The validation tests showed that single precision numerical noise generated an index of -5 when a pure, single wavenumber sine wave was used to generate 3D input data, tending to indicate therefore there is still some power at these scales as the spectrum is not as steep as -5 . Calculation of power spectrum at earlier times shows that before 23 Myrs, the index of the spectrum is steeper than -3 , but this rapidly softens to $-5/2$ as high density structure emerges around 25 Myrs. From $t=30$ Myrs onwards, the velocity power spectrum of the cloud complex has reached a steady state and is as shown in Fig. 10.

The velocity power spectra of Clump R is an order of magnitude less powerful than that observed in the cloud complex as a whole. The cube encompassing Clump R for the Fourier Transform was 10 pc on a side and power spectra of Clump R are hence reduced by a factor of 4^3 in order to allow direct comparisons between cloud and Clump spectra. Again the velocity power spectra has two inertial ranges over which the spectral indices are approximately constant, this time with a break between the two at $k = 10$ - notably the same physical scale of 1 pc. At length-scales longer than 1 pc (lower wavenumbers), the inertial range is again $-5/3$ - indicating consistent sampling of the same thermal instability flow in the warm stable medium in this smaller box. At shorter length-scales, typically inside the clump, the index is approximately -3 , not dissimilar to that simulated by others on that scale and below (Medina et al. 2014).

It is remarkable that a simulation that started out as a stationary diffuse cloud and that generates large-scale ordered flows, displays a long-lasting turbulence-like $-5/3$ spectrum on an inertial range across one decade of wavenumber, *even though there is no fully developed turbulence in this simulation and there was no driving scale in the initial condition*. What the simulation has generated is flow containing a “hierarchy of small-scale irregularities superimposed on larger-scale more systematic motions” – very much the definition of Larson-like turbulence (Larson 1981, and “1. Introduction” therein for the source of this quote). This result also makes it difficult to determine the nature of clumps, as what may appear turbulent is actually a signature of complex infall velocities. Previous authors have noted that clumps with clear signatures of infall are statistically indistinguishable from clumps with no such signatures (Traficante et al. 2018). The same authors noted that the observed non-thermal (i.e. supersonic) motions are not necessarily ascribed to turbulence acting to sustain gravity, but they may be due to the gravitational collapse at clump scales – precisely what we see here.

Given the extensive nature of the warm neutral medium, this result suggests that this index of $-5/3$ should extend to larger spatial scales than considered here - i.e.

¹ The interactive data language; https://www.harrisgeospatial.com/docs/using_idl_home.html

there is no physical reason for an inertial range limiting upper physical scale. It should be noted that fully developed turbulence, even in astrophysical scenarios, displays an inertial range over many orders of magnitude in k , for example in the magnetic fields of neutron stars (Wareing & Hollerbach 2009, 2010). Galactic-scale simulations have found that the correlation scale of the large-scale random flows, calculated from the velocity auto-correlation function, is on the order of 100 pc (Gent et al. 2013). This may or may not lead to a break in power spectra at this scale, but is larger than the scales considered here, lending support to our finding of structured, or correlated, flows on scales shorter than 100 pc. Further work is required to answer questions over how the large-scale turbulent nature of galaxies may be converted to correlated flows below the correlation length.

The lower physical scale limit of the turbulence-like inertial range is however a resolved physical characteristic of the models – specifically, the scale of the cold condensations produced by thermal instability. It should not shift to smaller physical size (higher wavenumber) with the use of greater resolution. Given the nature of the energy change across the phase boundary, with increasing infall velocity on the scale of a few km s^{-1} on the warm side of the boundary, rapidly decreasing to an order of magnitude lower velocities on the cold side of the boundary, it would be natural to call the \sim few pc scale of these cold dense clumps the “dissipative limit” of the turbulent velocity spectrum of the warm neutral medium.

The power spectra of density in the cloud complex peaks at $k = 8$. As noted previously, the size of the cube used for the Fourier Transform is 40 pc on a side so this is equivalent to 5 pc and in expected agreement with the 5 pc scale of the dense clumps in the cloud. There is some sign of an inertial range between $k = 8$ and $k = 40$ with an index around $-5/3$, reflective of the substructure in the clumps. Given there is structure throughout the cloud on the scale of 1 to 5 pc as shown in Figs. 7 and 8, this seems reasonable. At $k > 40$, there is a steepening of the power spectra, indicating relatively less smaller-scale structure. Calculation of density power spectrum at earlier times shows that before 23 Myrs, the spectrum is far less powerful and weakly peaked at large k on the small scale (\sim 1 pc) of the growing inhomogeneities (as well as an expected strong peak at the scale of the entire cloud complex). As structure grows in the simulation, the density power spectrum rapidly rises and steepens, although takes a longer period to display a steady state spectral index than the velocity power spectrum. From 35 Myrs onwards, the density power spectrum is in agreement with the snapshot spectrum shown here in Fig. 10, although rising in power (shifting directly upwards in the figure) as densities increase in the clumps.

Clump R displays a power spectra of density in agreement with this, with structure on the order a few pc (up to $k = 4$) before a steepening power spectra. If Clump R were spherical with radius 5 pc, we would expect a peak at $k = 2$ from this 10 pc box analysis, but as clearly shown in Fig. 9, the clump is anything but spherical. There is no inertial range, but the spectral index steepens from approximately $-5/2$, indicating that this clump, where self-gravity has taken over from the effect of the thermal instability, is not dissimilar to those simulated elsewhere (Medina et al. 2014). There are also similarities with observations of the

Perseus molecular cloud, where multi-phase density power spectra with indices of $-5/2$ and steeper are derived (Pingel et al. 2018).

Again, it is worth highlighting that the power spectra resulting from these simulations which start from a stationary initial condition, are not dissimilar from those that start from turbulent initial conditions, nor dissimilar to observed power spectra. There is also no evidence for the 0.29 pc resolution scale of the initial simulation in Paper IV – the spectra are smooth across k of 138 for the cloud complex and k of 34 for the Clump R spectra). If anything can be considered a ‘driving scale’ in these simulations, it is that 0.29 pc scale upon which the initial density inhomogeneities are introduced at $t = 0$. There is no evidence that this scale has dominated our simulations and it is very different to the 5 pc acoustic length scale of the warm stable medium that seems to be observed defining clump-scales here and sheet separation scales in the magnetic case (see Papers I and IV).

Further study is required to determine whether the use of power spectra can meaningfully discern between models of star formation, but these results indicate power spectra are a blunt tool for understanding the formation of molecular clouds. The results also cast doubt on any justification for the injection of driven turbulence in numerical models of molecular clouds, since it is apparent that our simulations naturally produce long-lasting turbulence-like power spectra from an ordered flow. The question of whether such flows can reproduce other observational features of the velocity and density dispersions, is left to a later paper.

7 RE-SIMULATING THE FINAL COLLAPSE OF THE MOST MASSIVE CLUMP

The most massive clump, Clump D, has been extracted and resimulated at even higher resolution (0.016 pc on the finest AMR level) in order to examine the collapse of the clump and confirm that it is gravitationally bound and Jeans unstable. On a short time scale of approximately 100,000 years, from $t=44$ Myrs to $t=44.1$ Myrs, the density in the clump rises steeply up to $n_H = 3.5 \times 10^6 \text{ cm}^{-3}$. 91% of the mass in the clump, equivalent to approximately $250 M_\odot$, is in the cold phase. The unstable envelope around the clump contains little more than one solar mass of material. The central pressure in the clump has risen to two orders of magnitude greater than the average pressure of the warm stable surroundings. An energy analysis of the simulated data reveals that the clump is strongly gravitationally bound - the clump has three times more gravitational energy than the sum of kinetic and thermal energy, making it also Jeans unstable. The apparent nature of the clump is very similar to that shown in Fig. 9, albeit with a far greater peak density. A Plummer-like profile is a good fit, but again substructure in the clump means there are large variations in different radial directions outward from the peak density.

In combination with the simulations presented earlier, we have conclusively demonstrated that thermally unstable diffuse material can evolve cold and dense structure which can be strongly influenced by gravity. This can lead to the eventual collapse of such structure under gravity, without the need to include any other physics or factors, e.g. pressure waves, shocks or collisions, although clearly these play a role

which can now be elucidated in future work. Remarkably, in the purely hydrodynamic case, the natural evolution of the diffuse unstable cloud produces a distribution of cold, dense clumps connected by long-lived filaments that would appear to have a characteristic size scale of 0.2 to 0.6 pc.

8 CONCLUSIONS

In this work, we set out to determine by the use of hydrodynamic simulation whether a molecular cloud structure evolved from diffuse, thermally unstable medium could ever lead to gravitationally collapsing structure, without the influence of any other physics (e.g. turbulence) or external disturbance (pressure wave, shock or collision).

Our previous work, at lower resolution of 0.29 pc or greater, had revealed that clumpy clouds form in the hydrodynamic case and corrugated sheet-like clouds, that in projection appear filamentary, form in the magnetic case. Neither set of previous simulations conclusively demonstrated gravitational collapse within such models of molecular clouds.

The suite of high-resolution simulations carried out here, with typically 0.078 pc resolution, but up to 0.016 pc resolution, have now conclusively demonstrated that thermal instability in a diffuse medium alone can generate cold and dense enough structure to allow self-gravity to take over and conclude the star formation process. The total time scale for this to happen is on the order of 40 Myrs, although the structure would only be considered a molecular cloud for the previous 15 Myrs. The final gravitational collapse sees density increase by 3 orders of magnitude on very short time scales of 10^5 years.

We have noted the following:-

- (i) Diffuse thermally unstable material evolves into a stable network of cold dense clumps multiply-connected by filaments, immersed in warm tenuous material.
- (ii) The filaments form and accrete as unstable gas falls in, with widths ranging from less than 0.26 pc as they first form, up to 0.56 pc and more after 6 Myrs.
- (iii) During the early evolution of the cloud complex, high densities in the filaments and proto-clumps caused by thermal instability driven flow can be mis-leading, in terms of applying automatic star particle injection routines. Convergent flow, energy analysis and gravitational potential conditions can all be satisfied, but accurate investigation reveals this to be a transient dynamical phase in the formation of the cloud complex, not gravitational collapse.
- (iv) Application of the FellWalker (Berry 2015) algorithm identifies 21 massive ($> 20 M_{\odot}$) clumps that have formed in this 3,000 M_{\odot} region of cloud.
- (v) The clumps formed have a size-scale of 5 pc or less, masses up to 300 M_{\odot} , internal temperatures of 10-30 K and internal velocity dispersions of 0.5 km s^{-1} or less. These physical characteristics are in agreement with the definition of clumps presented by Bergin & Tafalla (2007) and density distributions can be fitted by a Plummer-like profile (Whitworth & Ward-Thompson 2001).
- (vi) In agreement with previous models (see Micic et al. 2013, and references therein) the majority of clumps are not initially collapsing. The most massive clump has been investigated at a resolution of 0.016 pc and does collapse

under gravity, increasing its central density by 3 orders of magnitude on a time scale of 100,000 years.

(vii) Velocity power spectra of the cloud complex as a whole and an individual massive clump show spectral indices which are turbulence-like ($-5/3$) over a short inertial range (approximately one decade of wavenumber), even though the initial diffuse condition was stationary. This is the result of a large-scale flow with a hierarchy of small-scale structure, very much as predicted by Larson (1981). The wavenumber of the break-point in the spectrum corresponds to the 5 pc size-scale of individual clumps.

(viii) Power spectra of velocity and density are not dissimilar to simulations that employ turbulent initial conditions implying that 1D power spectra may not offer a meaningful tool to discern between models of star formation.

(ix) The most massive clumps eventually undergo runaway gravitational collapse with analysis determining that they are truly gravitationally bound and Jeans unstable.

Immediate future work will consider the effect of magnetic fields in this scenario, applying the same high resolution to MHD simulations (which have been run alongside this suite of simulations) and looking for gravitational collapse in the magnetic case, as well as explanations for the origins of striations (Tritsis & Tassis 2016), disconnections along filaments resulting in ‘integral-shapes’ (Stutz, Gonzalez-Lobos & Gould 2018) and the formation of strongly distorted magnetic fields, e.g. hour-glass field morphologies (Pattle et al. 2017). Other work will study the effect of various feedback mechanisms in this cloud complex, introducing a robust star-particle formation technique, sampling a realistic initial mass function in order to determine the star formation rate of this cloud complex.

ACKNOWLEDGMENTS

We acknowledge support from the Science and Technology Facilities Council (STFC, Research Grant ST/P00041X/1). The calculations herein were performed on the DiRAC 1 Facility at Leeds jointly funded by STFC, the Large Facilities Capital Fund of BIS and the University of Leeds and on other facilities at the University of Leeds. Data presented herein is available from <http://doi.org/10.5518/483>. We thank the anonymous referee for a detailed review of the manuscript which improved the presentation and flow of the manuscript considerably, and which enhanced the detail of a number of the results presented. We thank David Hughes at Leeds for the provision of IDL scripts which formed the basis of the power spectra analysis presented in this work. VisIt (VisIt Collaboration 2012) is supported by the Department of Energy with funding from the Advanced Simulation and Computing Program and the Scientific Discovery through Advanced Computing Program.

REFERENCES

- André P., Di Francesco J., Ward-Thompson D., Inutsuka S.-I., Pudritz R. E., Pineda J. E., 2014, in Beuther H., Klessen R. S., Dullemond C. P., Henning T., eds, *Protostars and Planets VI*. University of Arizona Press, Tucson, 914. p. 27

- Arzoumanian D. et al., 2019, *A&A*, 621, id.A42
- Ballasteros-Paredes J., Vázquez-Semadini E., Palau A., Klessen R. S., 2018, *MNRAS*, 479, 2112
- Bastien P., 1983, *A&A*, 119, 109
- Begum A., Stanimirović S., Goss W. M., Heiles C., Pavkovich A. S., Hennebelle P., 2010, *ApJ*, 725, 1779
- Bergin E. A., Tafalla M., 2007, *ARAA*, 45, 339
- Berry D. S., 2015, *Astronomy and Computing*, 10, 22
- Beuther H., Linz H., Henning T., eds, 2008, *ASP Conf. Ser.* Vol. 387. *Massive Star Formation: Observations Confront Theory*. Astron. Soc. Pac., San Francisco
- Birk G. T., 2000, *Physics of Plasmas*, 7, 3811
- Brühlweiler F. C., Freire Ferrero R., Bourdin M. O., Gull T. R., 2010, *ApJ*, 719, 1872
- Falle S. A. E. G., 1991, *MNRAS*, 250, 581
- Falle S. A. E. G., 2005, *Proceedings of the Chicago Workshop on Adaptive Mesh Refinement Methods*, Springer Lecture Notes in Computational Science and Engineering (Springer, New York, USA), 41, 235
- Hubber D. A., Falle S. A. E. G., Goodwin S. P., 2013, *MNRAS*, 432, 711
- Federrath C., Roman-Duval J., Klessen R. S., Schmidt W., Mac Low M.-M., 2010, *A&A*, 512, id.A81
- Field G. B., 1965, *ApJ*, 142, 531
- Fukue T., Kamaya H., 2007, *ApJ*, 669, 363
- Gatto A., et al. 2015, *MNRAS*, 449, 1057
- Gent F. A., Shukurov A., Fletcher A., Sarson G. R., Mantere M. J., 2013, *MNRAS*, 432, 1396
- Girichidis P., et al. 2015, *MNRAS*, 456, 3432
- Gnat O., Ferland G. J., 2012, *ApJS*, 199, article id. 20
- Godunov S. K., 1959, *Mat. Sbornik*, 47, 271
- Goicoechea J. R. et al., 2016, *Nature*, 537, 209
- Gómez G. C., Vázquez-Semadini E., 2014, *ApJ*, 791, article id. 124
- Gray W. J., Scannapieco E., 2011, *ApJ*, 733, 88
- Harper-Clark E., Murray N., 2009, *ApJ*, 693, 1696
- Heitsch F., Stone J. M., Hartmann L. W., 2009, *ApJ*, 695, 248
- Hennebelle P., Audit E., 2007, *A&A*, 465, 431
- Hennebelle P., Audit E., Miville-Deschênes M.-A., 2007, *A&A*, 465, 445
- Hennebelle P., Banerjee R., Vázquez-Semadini E., Klessen R. S., Audit E., 2008, *A&A*, 486, L43
- Hennebelle P., André P., 2013, *A&A*, 560, id.A68
- Heyer M. H., Brunt C. M., 2004, *ApJ*, 615, L45
- Icke V., van de Weygaert R., 1991, *QJRAS*, 32, 85
- Inoue T., Inutsuka S.-I., 2012, *ApJ*, 759, article id. 35
- Kainulainen J., Beuther H., Banerjee R., Federrath C., Henning T., 2011, *A&A*, 530, id.A64
- Kawamura A. et al., 2009, *ApJS*, 184, 1
- Kirk H., Klassen M., Pudritz R., Pillsworth S., 2015, *ApJ*, 802, article id. 75
- Koenig X. P., Leisawitz D. T., Benford D. J., Rebull L. M., Padgett D. L., Assef R. J., 2012, *ApJ*, 744, 130
- Körtgen B., Seifried D., Banerjee R., Vázquez-Semadini E., Zamora-Avilés M., 2016, *MNRAS*, 459, 3460
- Koyama H., Inutsuka S.-I., 2000, *ApJ*, 532, 980
- Koyama H., Inutsuka S.-I., 2002, *ApJ*, 564, L97
- Krumholz M. R., Burkhard B., 2016, *MNRAS*, 458, 1671
- Krumholz M. R., Matzner C. D., 2009, *ApJ*, 703, 1352
- Kurganov A., Tadmor E., 2000, *J. Co. Ph.*, 160, 241
- Larson R. B., 1981, *MNRAS*, 194, 809
- Li Z.-Y., Wang P., Abel T., Nakamura F., 2010, *ApJ*, 720, L26
- Lim A. J., Falle S. A. E. G., Hartquist T. W., 2005, *ApJ*, 632, L91
- Loren R. B., 1989, *ApJ*, 338, 925
- Mac Low M.-M., Klessen R. S., 2004, *Reviews of Modern Physics*, 76, 125
- Meagher A. J., Mukherjee M., Weaire D., Hutzler S., Banhart J., Garcia-Moreno F., 2011, *Soft Matter*, 7, 9881
- Medina S.-N. X., Arthur S. J., Henney W. J., Mellema G., Gazol A., 2014, *MNRAS*, 445, 1797
- Micic M., Glover S. C. O., Banerjee R., Klessen R. S., 2013, *MNRAS*, 432, 626
- Moeckel N., Burkert A., 2015, *ApJ*, 807, article id. 67
- Nejad-Asghar M., Ghanbari J., 2003, *MNRAS*, 345, 1323
- Offner S. S. R., Arce H. G., 2015, *ApJ*, 811, article id. 146
- Ostriker E. C., McKee C. F., Leroy A. K., 2010, *ApJ*, 721, 975
- Padoan P., Juvela M., Goodman A. A., Nordlund Å., 2001, *ApJ*, 553, 227
- Padoan P., Juvela M., Kritsuk A., Norman M. L., 2006, *ApJ*, 653, L125
- Panopoulou G. V., Psaradaki I., Skolidis R., Tassis K., Andrews J. J., 2017, *MNRAS*, 466, 2529
- Parker E. N., 1953, *ApJ*, 117, 431
- Pattle K., et al. 2017, *ApJ*, 846, article id. 122
- Peretto N. et al., 2013, *A&A*, 555, id.A112
- Pingel N. M., Lee M.-Y., Burkhard B., Stanimirović S., 2018, *ApJ*, 856, 136
- Porter D., Pouquet A., Woodward P. R., 1994, *Phys. Fluids*, 6, 2133
- Rogers H., Pittard J. M., 2013, *MNRAS*, 431, 1337
- Rogers H., Pittard J. M., 2014, *MNRAS*, 441, 964
- Shadmehri M., 2009, *MNRAS*, 397, 1521
- Smith R., Glover S. C. O., Klessen R. S., 2014, *MNRAS*, 445, 2900
- Solomon P. M., Rivolo A. R., Barrett J., Yahil A., 1987, *ApJ*, 319, 730
- Stanimirović S., Zweibel E. G., 2019, *ARAA*, 56, 489
- Stutz A., Gonzalez-Lobos V. I., Gould A., *MNRAS submitted*. arXiv:1807.11496
- Stiele H., Lesch H., Heitsch F., 2006, *MNRAS*, 372, 862
- Traficante A., Duarte-Cabral A., Elia D., Fuller G. A., Merello M., Molinari S., Peretto N., Schisano E., Di Giorgio A., 2018, *MNRAS*, 477, 2220
- Tritsis A., Tassis K., 2016, *MNRAS*, 462, 3602
- Truelove J. K., Klein R., McKee C. F., Holliman J. H. II, Howell L. H., Greenough J. A., 1997, *ApJ*, 489, L179
- Van Loo S., Falle S. A. E. G., Hartquist T. W., 2010, *MNRAS*, 406, 1260
- Van Loo S., Tan J. C., Falle S. A. E. G., 2015, *ApJ*, 800, article id. L11
- Vázquez-Semadini E., 1994, *ApJ*, 423, 681
- Vázquez-Semadini E., Gómez G.C., Jappsen A. J., Ballasteros-Paredes J., González R. F., Klessen R. S., 2007, *ApJ*, 657, 870
- VisIt Collaboration, 2012, in “High Performance Visualisation – Enabling Extreme-Scale Scientific Insight”, pp. 357-372
- Walch S. K., Naab T., 2015, *MNRAS*, 451, 2757
- Walch S. K., et al. 2015, *MNRAS*, 454, 238
- Wareing C. J., Hollerbach R., 2009, *Physics of Plasmas*, 16,

042307

- Wareing C. J., Hollerbach R., 2010, *Journal of Plasma Physics*, 76, 117
- Wareing C. J., Pittard J. M., Falle S. A. E. G., Van Loo S., 2016, *MNRAS*, 459, 1803; Paper I
- Wareing C. J., Pittard J. M., Falle S. A. E. G., 2017a, *MNRAS*, 465, 2757; Paper II
- Wareing C. J., Pittard J. M., Falle S. A. E. G., 2017b, *MNRAS*, 470, 2283; Paper III
- Wareing C. J., Pittard J. M., Wright N. J., Falle S. A. E. G., 2018, *MNRAS*, 475, 3598; Paper IV
- Whitworth A. P., Ward-Thompson D., 2001, *ApJ*, 547, 317
- Williams J. P., de Geus E. J., Blitz L., 1994, *ApJ*, 428, 693
- Wolfire M. G., Hollenbach D., McKee C. F., Tielens A. G. G. M., Bakes E. L. O., 1995, *ApJ*, 443, 152
- Zuo P., Li D., Peek J. E. G., Chang Q., Zhang X., Chapman N., Goldsmith P. F., Zhang Z.-Y., 2018, *ApJ*, 867, 13